Design and Numeric Evaluation of a Novel Axial-Flow Left Ventricular Assist Device

Koral Toptop and Kamuran A. Kadipasaoglu

Virtual design characteristics and performance of the first Turkish axial-flow left ventricular assist device (LVAD) are presented, with emphasis on rotor geometry. The patented rotor design includes a central flow channel carved inside the main block, which carries permanent magnets. A concentric rotor-stator gap minimizes the distance between respective magnets, improving electromagnetic efficiency and creating a second blood pathway. Dual sets of three helical blades, placed on the shaft and external surface of the rotor block, ensure unidirectionality. Hemodynamic performance was tested with computational fluid dynamics (CFD); and rotor-blade geometry was optimized, to maximize overall efficiency d and minimize backflow and wall shear stresses. For a shaft radius of 4.5 mm, rotor blade height of 2.5 mm, and blade inlet and exit metal angles of 67° and 32°, pump operation at the nominal head-flow combination (5 L/min and 100.4 mm Hg) was achieved at a rotor speed of 10,313 rpm. At the nominal point, backflow as percent of total flow was 7.29 and 29.87% at rotor inlet and exit, respectively; overall hydraulic efficiency reached 21.59%; and maximum area-averaged shroud shear was 520 Pa. Overall efficiency peaked at 24.07% for a pump flow of 6.90 L/min, and averaged at 22.57% within the flow range of 4–8 L/min. We concluded that the design satisfies initial rotor design criteria, and that continued studies with diffuser optimization and transient flow analysis are warranted. *ASAIO Journal* 2013; 59:230–239.

Key Words: left ventricular assist device, axial-flow heart pump, computational fluid dynamics, velocity triangle, turbomachinery electro-magnetic efficiency, hydraulic efficiency, drag coefficient, incidence, secondary flow pathway, magnet cylinder

The design and production of left ventricular assist devices (LVADs) in developing countries are a medical, technological, scientific, and economic imperative. This work was undertaken to construct and test the first axial-flow LVAD in Turkey. To reduce design complexities at the early developmental stages, a prototype was conceived as a second-generation LVAD to be implanted in the thoracic cavity, interposed between the left ventricular (LV) apex and the ascending aorta.[1]

In conventional designs, the hub-to-shroud gap is maximized to increase effective cross-sectional blood flow area (A_c). In this configuration, the distance between rotor and stator magnets decreases magnetic field intensity across the gap. To recover the resulting loss in motor power, either 1) the volume of magnets or the number of coil turns is increased, in which cases larger magnets increase device mass and size and increased coil turns lead to elevated electrical losses and/or overheating; or 2) permanent magnets are buried in the rotor blades, which limits available magnet volume (thus motor power), which is recoverable only by increasing the number of coil turns.

Innovative design features were incorporated in the current design so as to attain the desired hemodynamic performance at a lower power. Primary design criteria were pump size, hemodynamics, and hemocompatibility. Shaft speed was controlled to minimize wall shear stresses while eliminating stagnation points. Also, overall efficiency was maximized at the nominal design point while staying within anatomical constraints. Due to space limitations, only rotor design and optimization are described in this report, stator geometry having been selected based on convention[2] and its optimization considered the subject of subsequent analysis.

Methods

All symbols and subscripts are described in **Table 1** and **2**.

Design Concept

Inducer and diffuser blade geometries as well as rotor blade tip-to-shroud gap were assumed fixed. The inducer was designed (SolidWorks, Dassault Systems, Walton, MA) with four blades parallel to the flow axis (*i.e.*, inducer blade exit angle, $\alpha_1 = 0$), in order to prevent prerotation at rotor inlet. The diffuser was designed with five blades; the metal angles at inlet (β_{b3}) and exit (β_{b4}) were set at 66° and 0°, respectively, the latter in order to minimize whirl at pump exit.

The limitations in rotor magnet volume and losses in magnetic flux, both arising from flow area constraints, have been circumvented by transporting the primary flow path to the center of the rotor magnet cylinder. Blades were fixed to the centrally axial shaft (hub) and to the inside surface of the magnetic cylinder (tip). Smaller height blades were installed on the outside surface of the magnet cylinder to encourage forward flow in the secondary flow path between the magnet cylinder and the shroud (**Figure 1**). Rotor length and rotor magnet length (l_m) were taken as 40 mm and 10 mm, respectively, and rotor gap clearance was set at 0.2 mm for all blade designs.

From the Department of Biomedical Engineering, Bahcesehir University, Istanbul, Turkey.

Disclosure: The authors have no conflicts of interest to report.

This work was supported by Grant No. 111M243 from the Scientific and Technologic Research Council of Turkey (TUBITAK) and Grant No. 00706.STZ.2010-2 from the Turkish Ministry of Science, Industry and Technology.

Reprint Requests: Kamuran A. Kadipasaoglu, Bahcesehir University, Ciragan Caddesi No: 4 D-315, Besiktas, Istanbul, Turkey. Email: kamuran.kadipasaoglu@bahcesehir.edu.tr.

DOI: 10.1097/MAT.0b013e31828a6bc1

Table 1. Symbols

		Units
Angles (relative to axial direction)		
α	Absolute flow	Deg.
β_{b2}	Relative flow	Deg.
i	Incidence	Deg.
δ	Deviation	Deg.
Kinematic		
ν	Absolute velocity	m/s
w	Relative velocity	m/s
u	Linear velocity at medial plane	m/s
ω	Rotational speed	*rpm*
Geometric		
r	Radius	*m*
A	Area	m^2
c	Chord	*m*
s	Pitch	*m*
σ	Solidity	dim.less
κ	Rotor-to-diffuser drag coefficient Ratio (C_{Dr}/C_{Dd})	dim.less
λ	Diffuser-to-rotor solidity ratio (σ_d/σ_r)	dim.less
Hydrodynamic		
ρ	Density	kg/m^3
$\dot{m}$	Mass flow rate	kg/s
Q	Volumetric flow rate	m^3/s
ΔH	Pressure rise	*Pa*
T	Torque	*N.m*
X	Axial force at unit depth	kg/s^2
Y	Tangential force at unit depth	kg/s^2
D	Drag force at unit depth	kg/s^2
L	Lift force at unit depth	kg/s^2
Coefficients		
η	Efficiency	dim.less
C_D	Drag coefficient	dim.less
Other		
Δ	Change across two points	

Table 2. Subscripts

	Direction
u	Tangential
x	Axial
Station	
r	Rotor
d	Diffuser
Location	
1	Rotor inlet
2	Rotor outlet
3	Diffuser inlet
4	Diffuser outlet
Angles	
f	Fluid
b	Blade
Other	
i	Inlet
o	Outlet
p	Pump (all sections)
m, mean	Mean
c	Cross-sectional
h	Hydraulic
nom	Nominal

Design Variables and Constraints

Independent design variables were rotor speed (ω) and rotor blade geometry. The parameters relating to rotor geometry were tip (r_t) and hub (r_h) radii (which, together, defined A_c and mean blade radius, r_m), and rotor blade metal angles at inlet (β_{b1}) and exit (β_{b2}). Dependent design variables were shaft torque (T), pump flow (Q) and head (ΔH), overall hydraulic efficiency (η_h), area-averaged shroud shear stresses (SS_{sh}), and backflow (BF) and forward flow (FF) expressed as percent of total forward flow.

Nominal pump operation point was set at Q = 5 L/min and ΔH= 100 mm Hg. Minimum acceptable value for η_h was 20%. Maximum allowable limit of SS_{sh} was 550 Pa to prevent hemolysis[3]; and those for BF were 15% and 35% at rotor inlet and outlet, respectively, to minimize turbulence.

Theoretical Calculations

Torque was obtained from fluid momentum change across rotor blades[4,5]

$$T = \rho Q r_m \Delta v_{ur} \tag{1}$$

where Δv_{ur}, the change in fluid tangential velocity across rotor blades, was obtained from velocity triangles (**Figure 2A**)

$$\Delta v_{ur} = u + v_x\left[\tan(\alpha_1) - \tan(\beta_{f2})\right] \tag{2}$$

Tangential velocity at the median plane was defined as $u = \omega r_m$; and fluid exit angle from rotor blades was assumed $20 < \beta_{f2} < 30$. Axial fluid speed, v_x, was determined from flow rate and area $\left(v_x = \frac{Q}{A_c}\right)$. Torsional-to-hydraulic power transfer was expressed using Euler work equation

$$T.\omega = \frac{1}{\eta_\eta}\Delta H.Q \tag{3}$$

Combining **Equations 1** and **2**

$$\Delta H = \eta_h \rho u \Delta v_{ur} \tag{4}$$

and

$$\omega^2 - \frac{\tan(\beta_{f2})Q}{A_c r_m}\omega - \frac{\Delta H}{\eta_h \rho {r_m}^2} = 0 \tag{5}$$

Hydraulic Efficiency

From force balance (**Figure 2B**), pressure rise (ΔP) across the blade (rotor or diffuser) was expressed as

$$\Delta P = \rho v_x \Delta v_u \tan(\beta_m) - \frac{\rho C_D \sigma {v_x}^2}{2\cos^3(\beta_m)} \tag{6}$$

where ρ is fluid density,σ is rotor blade solidity (chord–pitch ratio), and C_D is drag coefficient. Mean fluid angle β_m was defined as

$$\beta_m = \tan^{-1}\left[\frac{\tan(\beta_{fi}) + \tan(\beta_{fo})}{2}\right] \tag{7}$$

where the subscripts i and o refer to blade inlet and outlet, respectively. Kinetic energy rise (ΔKE) across the rotor was calculated assuming constant A_c

$$\Delta KE = \rho\frac{\left({v_{uo}}^2 - {v_{ui}}^2\right)}{2} \tag{8}$$

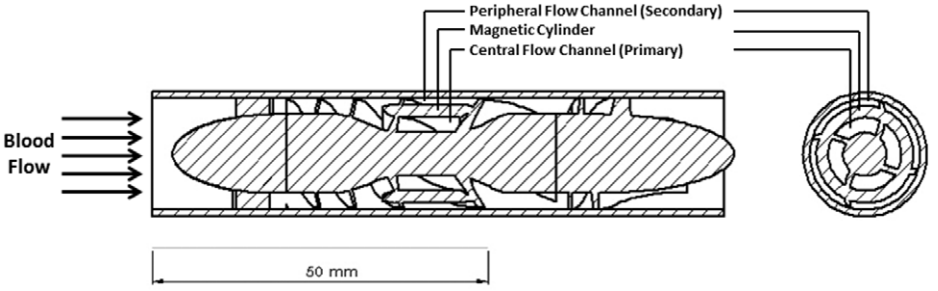

Figure 1. Cross-sectional side (left) and front views of the left ventricular assist device.

Blade pressure losses caused by drag forces were obtained from Bernoulli equation

$$h_{loss} = \Delta H - (\Delta P + \Delta KE) = \frac{\rho v_x^{\,2}}{2} \frac{\sigma C_D}{\cos^3(\beta_m)} \tag{9}$$

Pump efficiency was formulated as

$$\eta_h = 1 - \frac{h_{loss,rotor} + h_{loss,diffuser}}{\Delta H} \tag{10}$$

Efficiency was expressed as a function of Q, and maximized with respect to Q by *setting* $\frac{\delta \eta_h}{\delta Q} = 0$ (**Appendix**)

$$\sum_{k=0}^{8} \left\{ Q@\eta_{\max}{}^{(8-k)} \left(u\, A_c\right)^k \left[P_{[r,(9-k)]} - \left(\frac{\lambda}{\kappa}\right)^2 P_{[d,(9-k)]} \right] \right\} = 0 \tag{11}$$

where $Q@\eta_{\max}$ is the real root of **Equation 6** within range [3 < Q(L/min) < 10], which maximized η_h. Diffuser-to-rotor solidity ratio $\left(\lambda = \frac{\sigma_d}{\sigma_r}\right)$ was obtained from blade geometry, and the 1×9 arrays P_r and P_d are functions of β_{f2} (**Appendix**). The rotor-to-diffuser drag coefficient ratio ($\kappa = \frac{C_{Dr}}{C_{Dd}}$) was calculated after computational fluid dynamics (CFD) results became available (Section 2.6). **Equation 4** was written separately for rotor and

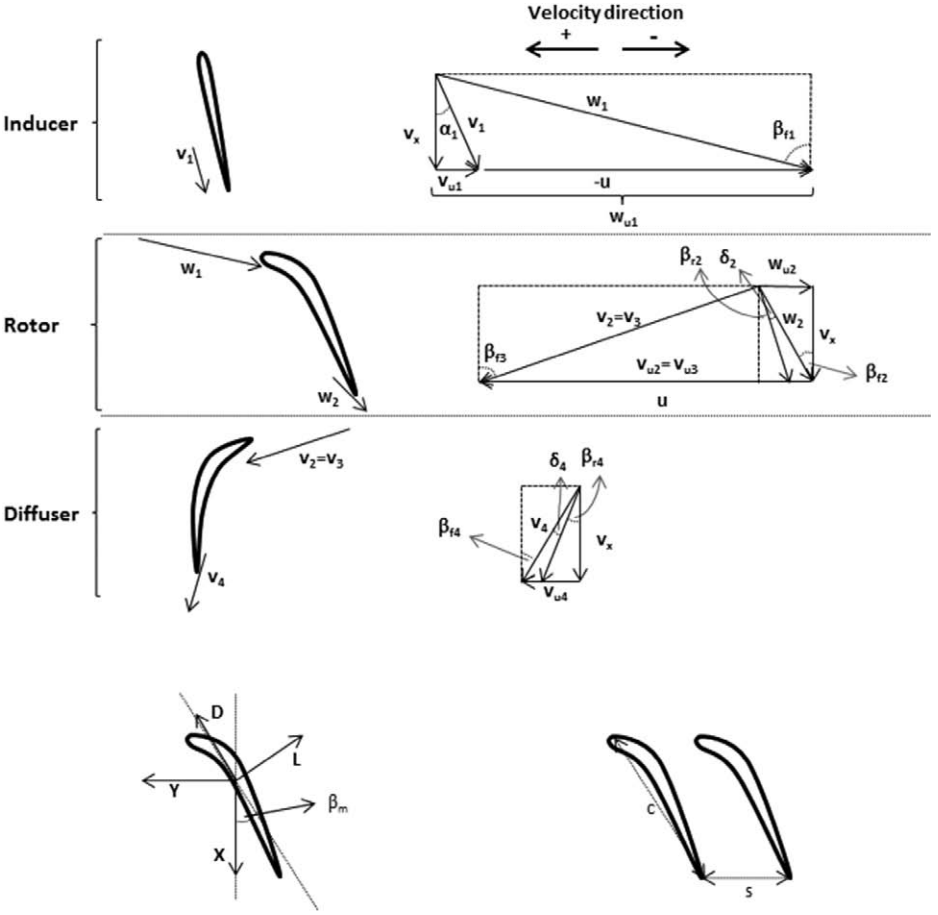

Figure 2. **A**: Velocity triangles at inlet and outlet of the inducer, rotor, and diffuser frames (top). **B**: Forces exerted on the blade and blade geometry. D, drag; L, lift; X, axial force on blade; Y, tangential force on blade; c, chord; s, pitch.

diffuser and the resulting equations were combined with **Equation 5**. After rearranging, rotor drag coefficient was expressed as

$$C_{Dr} = 2\kappa\,\rho\frac{{A_c}^2}{\sigma_\sigma}\frac{\left(1-\eta_\eta\right)}{\left(\frac{\kappa}{\cos^3(\beta_{mr})}+\frac{\lambda}{\cos^3(\beta_{md})}\right)}\frac{\Delta H}{Q^2} \quad (12)$$

and plotted as a function of Q.

Motor Calculations

Motor battery voltage and armature resistance, R, were accepted as 12 Volts and 0.011 Ohm, respectively. Armature current range was selected as $0.29 < i_a$ (Amp) < 0.37. Neglecting mechanical losses ($\eta_m = 1$), torque constant K_b was calculated by substituting[6]

$$T = K_b i_a \quad (13)$$

in **Equation 1** and rearranging

$$K_b = \rho r_m Q\frac{\frac{Q}{A_c}\left[tan(\alpha_1)-tan(\beta_{f2})\right]+\omega r_m}{\eta_m\ i_a} \quad (14)$$

The number of stator coil turns, *N*, was estimated from

$$N = \frac{K_b}{2\pi r_m l_m B_g} \quad (15)$$

Where B_g, magnetic field intensity at fluid gap, was assumed to be a function of magnet material (Nd-Fe-B, N48-40 grade) and pump body material (titanium).

Design Iterations

Beginning with η_h = 25% at the nominal pump operation point (Q = 5 L/min and ΔH = 100 mm Hg) and varying β_{f2}, r_{hub}, and r_{tip} within the specified flow range, corresponding values of ω were calculated from **Equation 3** using Matlab (The Mathworks, Natick, MA). Knowing and Q, fluid attack angle at rotor inlet ($\beta f1$) was calculated from velocity triangles (**Figure 2A**). Initially, rotor leading edge metal angle (β_{b1}) was equated to $\beta f1$, assuming zero rotor incidence ($i_r = \beta_{f1} - \beta_{b1}$). Finally, K_b and N were solved from **Equations 7** and **8**, respectively.

The virtual prototype (SolidWorks) was fed in a commercial Computational Fluid Dynamics software (CFD, ANSYS Inc., Canonsburg, PA), which computed the nominal values (at Q = 5 L/min, designated with the subscript "nom" from here on) of BF in primary and secondary flow channels at rotor inlet and exit, $SS_{sh,nom}$, ΔH_{nom}, and T_{nom}. The value of ω was iterated in CFD until experimental and nominal values of ΔH converged. At this point, η_{nom} was calculated from **Equation 2**. This provided the first ω -Q- ΔH- η_h combination of the actual characteristic performance curve of the pump. For the range of $0 < Q(L/min) < 10$, the η*h*-Q and ΔH-Q plots for constant ω were obtained in Matlab, at increments of 0.5 L/min. The flow rate, which maximized η_h, was identified as $Q@\eta_{max}$ and used for solving **Equation 6** (Section 2.4). Mean value of η_h for the operational range was calculated from

$$\eta_{mean} = \frac{\int_{Q\min}^{Q\max}\eta_h(Q)dQ}{(Q_{max}-Q_{min})} \quad (16)$$

The effect of rotor trailing (β_{b2}) and leading (β_{b1}) edge metal angles was tested in Models 1A–1F and 2A–2D, respectively. The effect of A_c on flow field and performance was tested in Model 3A. The respective values of β_{b2}, β_{b1}, and A_c, for which η_{max} was highest, were selected as the optimum for that design variable.

Computational Fluid Dynamic Analysis

Fluid domain was discretized into an 8-million-cell mesh to solve momentum and Navier–Stoke equations. Assuming turbulent characteristics at rotor inlet and across diffuser blades (Re > 10,000), k-ε turbulence model was adopted; and in order to locate the nodes as close to the viscous sublayer as possible, enhance wall treatment was used.

Left ventricular assist device flow domain was divided into three zones representing inducer, rotor, and diffuser. Frame rotation was applied to rotor zone, and rotor blade boundaries were defined as rotationally moving walls with zero relative velocity. All other surface boundaries were defined as nonslip stationary walls. Pump inlet and outlet cross-sections were defined as mass-flow inlet and pressure outlet, respectively; and boundary intersections at rotor inlet and outlet were defined as interface. Shroud shear stresses were averaged over areas where shear exceeded 400 Pa.

Results

Following the methodology described in Design Iterations, blade geometry optimization was conducted at the nominal design point.

Initial Shaft Speed and Blade Height

To approximate the starting point for blade geometry optimization by CFD, **Equation 3** was manipulated using Matlab. When A_c was augmented 30% by increasing blade tip height from 7 to 8 mm, ω changed from 9,923 to 8,627 rpm (–13%; **Table 3**).This, however, shifted $Q@\eta_{max}$, from 9.73 to 14.00 L/min (+44%), *i.e.*, farther away from the nominal flow. The location of $Q@\eta_{max}$ shifted right by ~20% with each 10% increase in A_c. Increasing theoretical fluid exit angle (β_{f2}) from 20° to 30° (+50%) brought $Q@\eta_{max}$ left by ~8%, while increasing ω by only 1–2% (**Table 3**). To begin CFD iterations, r_t and r_h were selected as 4 and 7 mm, respectively, and ω was set at 10,122 rpm.

Motor Calculations

At this speed, shaft torque was $3.3 < T(mN\text{-}m) < 4.2$ at the design point. With K_b = 11.4 mN-m/Amp and N = 9 turns/cm stator length, corresponding pump power range was $3.49 < W$ (Watts) < 4.44.

Design Iterations

Fluid attack angle at rotor inlet (β_{f1}) was determined as 81° from velocity triangles; and rotor blade attack angle (β_{b1}) was initially set at this value.

Table 3. Initial Matlab Calculations with Preliminary Values of Design Parameters

r_{tip} (*mm*)	r_{hub}(mm)	β_{f2} (Deg)	ω (rpm)	Q @ η_{max} (L/*min*)	T (×10-3N.m)	K_b(×10^{-3}N.m/Amp)
6	4	30	11,968	5.54	3.5	9.5
7	4	20	9,923	9,73	4.3	11.5
7	4	30	10,044	8.96	4.2	11.4
8	4	20	8,627	14.00	4.9	13.2
8	4	30	8,700	12.90	4.9	13.1
7	5	20	10,000	7,13	4.2	11.4
7	5	30	10,167	6.59	4.2	11.2
8	5	20	8,655	11.46	4.9	13.2
8	5	30	8,744	10.53	4.9	13.1

β_{f2}, theoretical fluid angle at rotor exit; ω, shaft speed; K_b, DC motor torque constant; Q@η_{max}, flow at maximum efficiency; r, rotor blade radius; T, torque.

Optimization of blade geometry at rotor exit. Remaining Model 3A was created. Reduced A_c not only lowered BF_{ri}

Table 4. Optimization of Rotor Blade Exit Angle, *β*b2, in Prototypes 1A–1F

	β_{b2} (Deg)	BF_{ro} (%)	η(%)	η_{max} (%)	Q @ η_{max} (L/min)	ΔH(mm Hg)	T (×10^{-3}N.m)
1A	37°	32.69	19.00	22.62	7.60	101.8	5.593
1B	32°	32.92	18.38	22.81	8.20	102.4	5.837
1C	23°	34.44	17.47	22.38	8.60	106.4	6.383
1D	18°	35.04	17.00	21.95	9.00	107.0	6.596
1E	14°	36.91	16.85	21.31	9.20	107.2	6.828
1F	0°	35.23	14.93	19.5	9.35	96.8	6.800

For all models, β_{b3} = 66°; β_{b4} = 0° , r_t/r_h = 7/4 mm. All values are for ω = 10,122 rpm, Q = 5 L/min, and β_{b1} = 81°.
$BF_{ro,}$ backflow at rotor outlet; Q @ η_{max}, flow at maximum efficiency.

at the Q_{nom}, rotor blade trailing angle was increased stepwise, starting from β_{b2} = 0° (**Table 4**). Shaft torque and pump head were observed to peak in Model 1E with β_{b2} = 14° (T_{nom} = 6.828 mN-m, ΔH_{nom} = 107.2 mm Hg), but η_{nom} was highest (= 19%) and backflow at rotor outlet was lowest ($BF_{ro,\ nom}$ = 32.69%) in Model 1A with β_{b2}= 37°. On the other hand,η_h -Q curve peaked in Model 1B with β_{b2} = 32°, while maximum attainable efficiency η_{max} = 22.81% occurred at $Q@\eta_{max}$ = 8.20 L/min. In Models 1A and 1E, highest η_{max} coincided with 7.60 and 9.20 L/min, respectively (**Figure 3**).

Optimization of blade geometry at rotor inlet. Continuing with Model 1B at the nominal flow rate, CFD iterations of blade attack angle, β_{b1}, were initiated. Backflow at rotor inlet was observed to minimize ($BF_{ri,nom}$ = 6.88%) as β_{b1} was lowered to 74° (Model 2A); but η_{nom} (20.74%),ΔH_{nom} (108.7 mm Hg), and T_{nom} (5.837 mN-m) maximized when β_{b1} was further lowered to 67°, 64.5°, and 58°, respectively (**Table 5**). The peak of the η_h -Q curve was highest in Model 2B (**Figure 4**), with η_{max} = 24.33% (6.7% improvement over Model 1B) observed at Q@η_{max} = 7.60 L/min (0.20 L/min closer to Q_{nom} *versus* Model 1B).

Velocity streamlines exhibited no prerotation at rotor inlet, no whirl at diffuser exit, and minimal disturbance at magnet inlet and exit (**Figure 5**). Flow was measured to split smoothly between central (through the magnetic cylinder) and peripheral (through the magnet-coil gap) channels of Model 2B (**Table 6**). Approximately 10% [479.8/(479.8 + 4331.8)] of the total flow passed through the peripheral channel, where total backflow accounted for 9.59% (47.9/499.5) of forward flow. Maximum area-averaged shroud stress was 514 Pa.

Optimization of rotor blade height. In a last iteration, r_h of Model 2B was increased from 4 mm to 4.5 mm, and by 51% (from 13.4 to 6.56) and BF_{ro} by 11% (from 32.92 to 29.16), but also decreased ΔH_{nom} by 12% (from 108.4 to 95.9 mm Hg, **Table 7**). Increasing ω from 10,122 to 10,313 rpm (+2%) recovered ΔH_{nom} back to 100.9 mm Hg with an associated increase in maximum mean shear from 514 Pa to 520 Pa (+1.2%). At this speed, η_{nom} was 21.59% (up by 4.1% *versus* Model 2B). Velocity streamlines improved *versus* Model 1B, particularly between the rotor blades (**Figure 5**). Maximum attainable efficiency of η_{max} = 24.07 occurred at Q@η_{max} = 6.90 L/min. Within the 4 < Q(L/min) < 8 range, η_{mean} was 22.57% (6.23% below η_{max} and 4.54% above η_{nom}) and rotor drag coefficient varied within the range 0.14 < C_{Dr} < 0.158.

Discussion

The computational design process of a novel axial-flow LVAD is presented with particular emphasis on the optimization of rotor geometry under steady-state flow conditions. Bearing design and inducer-rotor and rotor-diffuser gap hemocompatibility effects were omitted from the present work, while only superficial attention was given to magnet design and electromagnetic power feasibility.

Hydraulic Efficiency

Primary design objective was the maximization of rotor hydraulic efficiency (η_{nom}) at the nominal design point. To this end, an attempt was made not only to increase the maximum attainable efficiency (η_{max}), but also to shift the entire efficiency curve along the flow axis so that the flow which maximized efficiency (Q@η_{max}) coincides with nominal flow. It was also desired to have as flat a η_h -Q

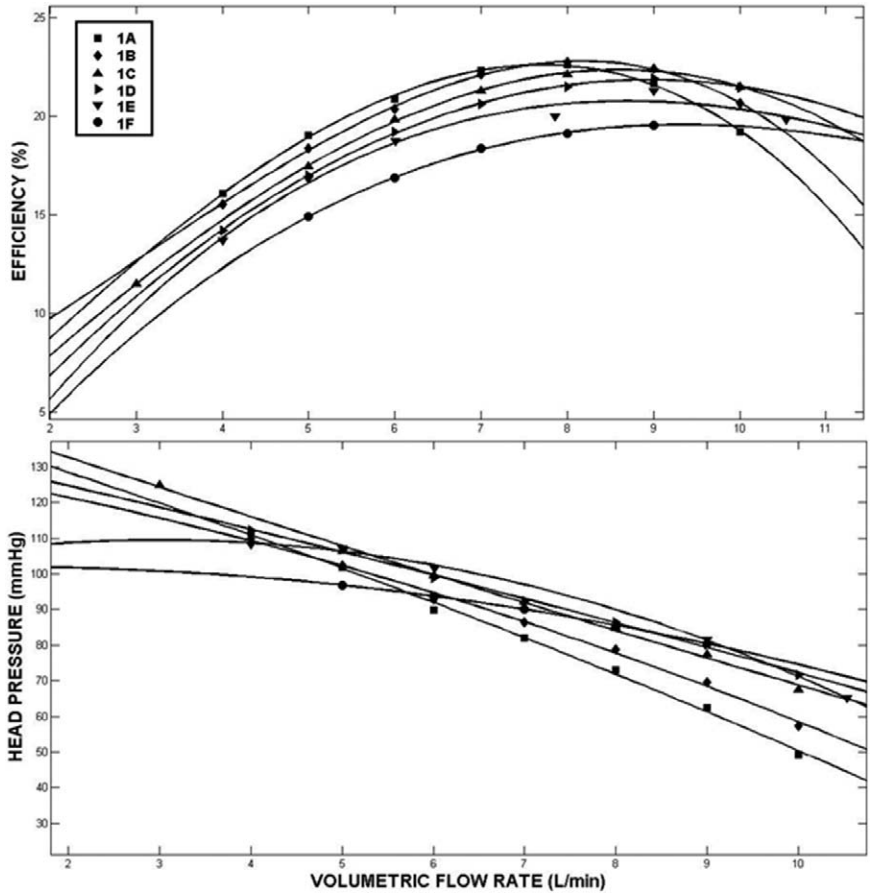

Figure 3. Computational fluid dynamics data for efficiency *vs.* flow (top); and for head pressure *vs.* flow (bottom) for prototypes 1A to 1F.

Table 5. Optimization of Rotor Blade Inlet Angle, βb1, in Prototypes 2A–2D

	β_{b1} (Deg)	BF_{ri} (%)	η_h (%)	η_{max} (%)	Q @ η_{max} (L/min)	ΔH(mm Hg)	T (×10^{-3}N.m)
1B	81°	-	18.38	22.81	8.20	102.4	5.837
2A	74.0°	6.88	20.01	20.33	6.00	96.4	5.480
2B	67.0°	13.4	20.74	24.33	7.60	108.4	5.480
2C	64.5°	14.9	20.17	24.05	7.85	108.7	5.647
2D	58.0°	17.42	18.38	22.81	8.05	102.4	5.837

For all models, β_{b2} = 32°; β_{b3} = 66°; β_{b4} = 0°; *and* r_t/r_h = 7/4 mm. All values are for ω = 10,122 rpm and Q = 5 L/min.
BF_{ri}, backflow at rotor inlet; Q @ η_{max}, flow at maximum efficiency.

curve as possible so that a relatively wide range of flow values yield efficiencies close to η_{max}. The latter condition particularly mattered since pump flow would be fluctuated for clinical purposes.[7] Indeed, in Model 3A, η_{mean} was only 6.23% below η_{max}, which occurred only 1.9 L/min to the right of Q_{nom} (**Table 7**).

Rotor Exit

Increasing blade trailing angle at rotor exit, β_{b2} an important parameter affecting pump performance in terms of head, torque, and flow, reduces the tangential component of exiting fluid velocity, hence the fluid attack angle (β_{f3}) at diffuser inlet (**Figure 2A**). CFD results showed that increasing β_{b2} effectively decreased backflow and steadily increased η_{max} (**Table 4**). Model 1B with β_{b2} = 32° was selected as its η_{max} = 22.81% was highest among other geometries (**Figure 3**). Associated losses in η_{nom} (19.00 to 18.38%), head (107.2 to 101.8 mm Hg), and torque (6.828 to 5.593 mN-m) were accepted in hopes of subsequent recovery by manipulating A_c.

Rotor Inlet

At the inducer–rotor interface, visualization of fluid streamlines by CFD illustrated the relationship between rotor incidence, i_r, and backflow (**Figure 6**). Velocity vectors (arrows) show forward (right) moving fluid around the inducer (horizontal on the left-hand side of each frame) toward the leading edge of the rotor blade (diagonal on the upper-mid region of each frame). As β_{b1} is reduced,

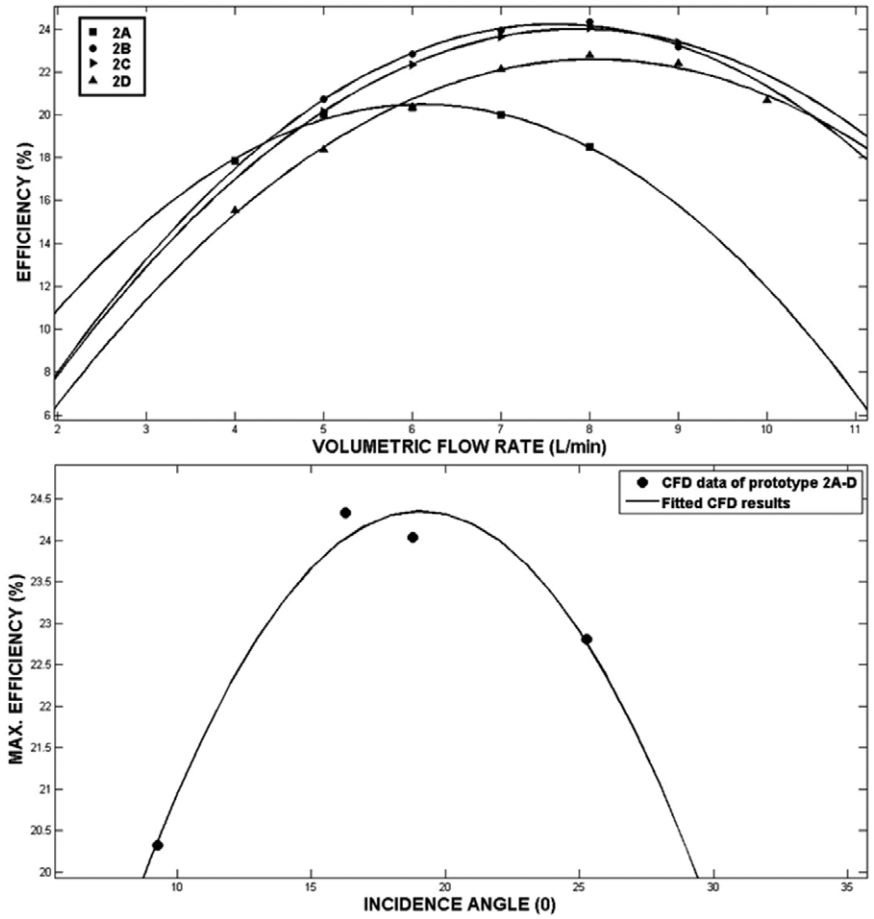

Figure 4. Computational fluid dynamics data of efficiency *vs.* flow for prototypes 2A–2D.

rotor blade rotated clockwise and incidence increased. The boundary layer progressively separated from the inducer surface and percent backflow between two adjacent rotor blades increased (arrows pointing left, against the flow). Backflow was accentuated in the radial direction, from mid-plane (left column) to shroud (right column) as the blade radius, hence tangential velocity increased. Clearly, flow patterns were smoother in Model 2A (**Figure 6**, top row; I = 7°) than in Model 2B (**Figure 6**, second row; I = 14°), as confirmed by the 94% higher backflow (6.88 *versus* 13.4) in the latter model (**Table 5**). However, since η_{max} and η_{nom} were highest with β_{b1} = 67°, Model 2B was selected, again, in anticipation of reduced backflow through subsequent optimization of A_c.

Blade Height

As expected, increasing r_{hub} in Model 3A reduced $BF_{ri,nom}$ and $BF_{ro,nom}$ (**Figure 5**; **Table 7**) possibly because the hub-to-tip pressure gradient was lowered, better aligning velocity streamlines. But the associated reduction in A_c caused v_x to increase, therefore β_{f1} to decrease (**Figure 2A**), which led to a slightly smaller rotor incidence. Considering data presented in **Table 4**, a reduction in rotor incidence angle may entail an increase in η_{max} within that range (moving from Model 2B to 2A), although data are insufficient to make that interpolation. On the other hand, reducing A_c is always associated with a significant drop in ΔH_{nom} (108.4 mm Hg to 95.9 mm Hg with 0.5 mm increase of r_h, **Table 7**). A less costly alternative would be to increase β_{b2}, which forces Q@η_{max} left, toward the design point (**Equation 6**); and the accompanying drop in ΔP would not be as much (**Table 4**) as it was when r_h was increased (**Table 7**). Further, respective pressure losses can be compensated by a smaller increase in shaft speed, inducing a smaller rise in shroud shear.

It should also be remembered that overall efficiency can be optimized by modifying diffuser blade leading edge angle (*i.e.*, manipulating diffuser incidence), which may prove a more practical design strategy for improving efficiency than modifying rotor deviation, an issue which will be addressed in subsequent studies.

Conclusion

This is the first of two reports on the virtual design and testing of a new Turkish axial-flow LVAD. Iterative optimization led to the geometry of Model 3A, which satisfied design criteria associated with flow patterns (hemolysis) and hemodynamics (physiology) within the size (anatomy) and power (electromagnetism) constraints. The focus of the subsequent

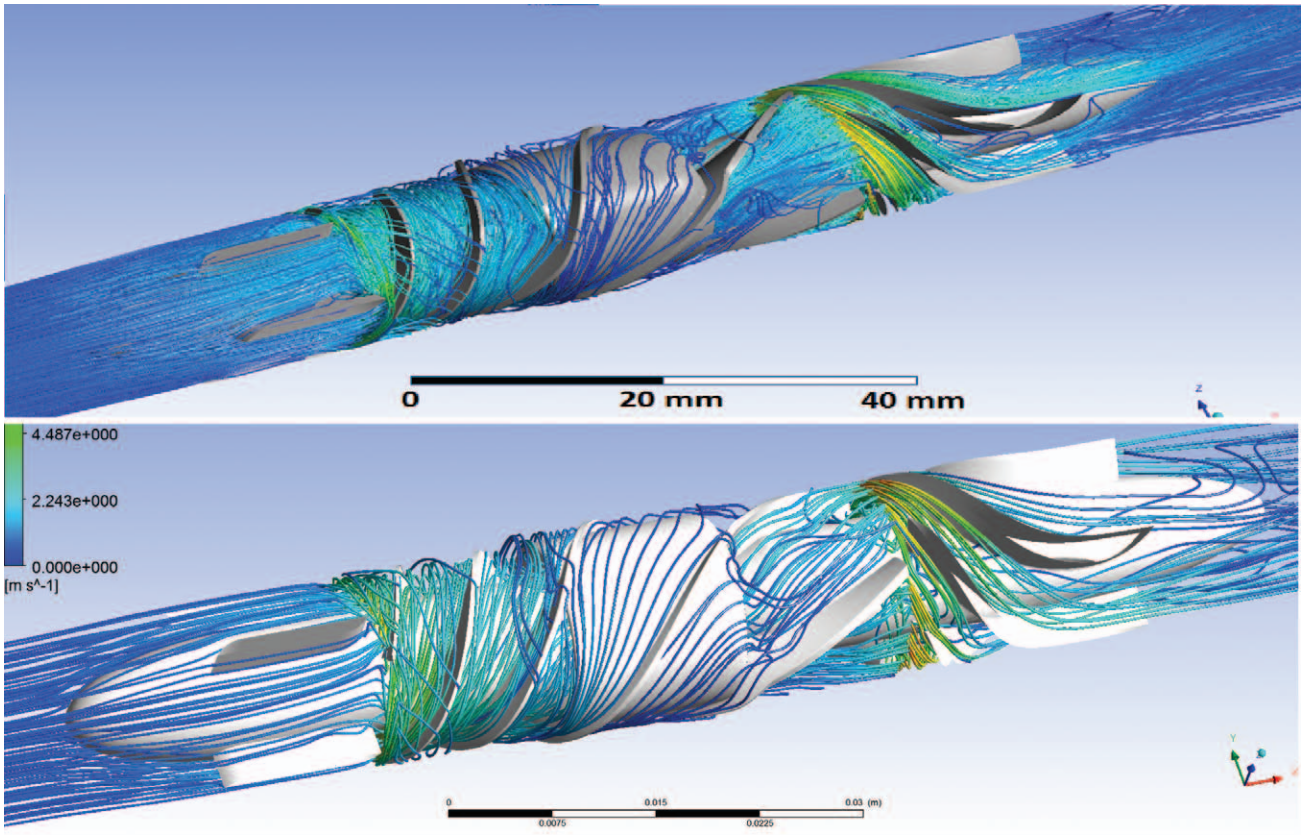

Figure 5. Velocity streamlines of Models 2B (top) and 3A. ω = 10,122 rpm, Q = 5L/m.

Table 6. Flow Rates in (Central or Primary) and Around (Peripheral or Secondary) Magnet Cylinder in Model 2B

Flow Path	BF_{ri} (ml/min)	FF_{ri} (ml/min)	BF_{ri}/FF_{ri} (%)	BF_{ro} (ml/min)	FF_{ro} (ml/min)	FF_{me}/TF (%)
Peripheral	47.9	499.50	9.59	40.3	479.80	9.97
Central	98.6	4,354.90	8.39	6.2	4,331.80	-

All values are for ω = 10,122 rpm and Q = 5 L/min.
BF_{ri}, Backflow at rotor inlet; BF_{ro}, backflow at rotor outlet; *F*,total flow; FF_{me}, forward flow external to magnet; FF_{ri}, forward flow at rotor inlet; FF_{ro}, forward flow at rotor outlet.

Table 7. Effect of Reducing Effective Flow Annulus Area, Ac, by Increasing r_{hub}

Model	r_{hub} (mm)	ω (rpm)	BF_{ri} (%)	BF_{ri} (%)	ΔH (mm Hg)	SS_{mean} (Pa)	η_h (%)	η_{mean} (%)	Q @ η_{max} (L/m)
2B	4.0	10,122	13.4	32.92	108.4	450	20.74	-	7.6
3A	4.5	10,122	6.56	29.16	95.9	514	21.71	22.57	6.9
	4.5	10,313	7.29	29.87	100.9	520	21.59	-	6.9

All values (except the last two columns) are for Q = 5 L/min. β_{b1} = 67°; β_{b2} = 32°; β_{b3} = 66°; β_{b4} = 0°; r_t = 7 mm.

report will be stator geometry optimization (including axial and radial gaps), while motor and bearing design will continue in parallel.

Results are presented with the understanding that all assessments should be repeated under transient conditions in order to have clinical bearing as the pump speed will be undulated. Also, pump geometry cannot be considered final until present computational findings are validated in physical (mock circuit, PIV) and biological (animal experiments and clinical studies) performance tests on physical prototypes.

Figure 6. Projection of velocity vectors for rotor blade inlet section at mid-plane (left column) and tip (right column) of the blade. Rows from top to bottom represent prototypes 2A through 2D.

Appendix

From trigonometric relations (**Figure 2A**)

$$cos^{-3}(\beta_m) = \left\{tan^2(\beta_m) + 1\right\}^{3/2} \tag{17}$$

For rotor and diffuser blades, respectively

$$cos^{-3}(\beta_{mr}) = \frac{\left\{\left[\gamma + tan(\alpha_1) + tan(\beta_{f2})\right]^2 + 4\right\}^{3/2}}{8} \tag{18}$$

$$cos^{-3}(\beta_{md}) = \frac{\left\{\left[\gamma + tan(\beta_{f4}) - tan(\beta_{f2})\right]^2 + 4\right\}^{3/2}}{8} \tag{19}$$

where $\gamma = \frac{u}{v_x}$. Substituting into the efficiency formula

$$\eta_p = 1 - \frac{f_r + f_d}{g} \tag{20}$$

where

$$f_r = C_{Dr}\sigma_r\left[(\gamma + X)^2 + 4\right]^{3/2} \tag{21}$$

$$f_d = C_{Dd}\sigma_d\left[(\gamma + Y)^2 + 4\right]^{3/2} \tag{22}$$

$$g = 16\left(\gamma^2 + \gamma Z\right) \tag{23}$$

and

$$X = tan(\alpha_1) + tan(\beta_{f2}) \tag{24}$$

$$Y = tan(\beta_{f4}) - tan(\beta_{f2}) \tag{25}$$

$$Z = tan(\alpha_1) - tan(\beta_{f2}) \tag{26}$$

Taking the derivative of η_p with respect to Q

$$\frac{d\eta_p}{dQ} = \frac{\partial\eta_p}{\partial\gamma}\frac{\partial\gamma}{\partial Q} \tag{27}$$

where

$$\frac{\partial\gamma}{\partial Q} = -\frac{A_c u}{Q^2} \tag{28}$$

and

$$\frac{\partial\eta_p}{\partial\gamma} = \frac{1}{g^2}\left[\left(f_r + f_d\right)\frac{dg}{d\gamma} + \left(\frac{df_r}{d\gamma} - \frac{df_d}{d\gamma}\right)g\right] \tag{29}$$

Executing the derivatives, rearranging and equating to zero, an 8th order polynomial in $Q@\eta_{max}$ is obtained

$$\sum_{k=0}^{8}\left\{Q@\eta_{\max}{}^{(8-k)}\left(u\,A_c\right)^k\left[P_{[r,(9-k)]}-\left(\frac{\sigma_d\,C_{Dd}}{\sigma_r\,C_{Dr}}\right)^2 P_{[d,(9-k)]}\right]\right\}=0 \tag{30}$$

where

$$P_r = P(N,Z), N = X \tag{31}$$

$$P_d = P(N,Z), N = Y$$

and

$$P=\begin{bmatrix}1\\ 4Z\\ \left(4Z^2-6N^2+6NZ-12\right)\\ \left(-4N^3-12N^2Z+12NZ^2-24N-24Z\right)\\ \left(9N^4-28N^3Z+9N^2Z^2-96NZ+36N^2\right)\\ (12N^5-12N^4Z-4N^3Z^2-72N^2Z-24NZ^2\\ \quad +96N^3+192N-96Z)\\ (4N^6+6N^5Z-6N^4Z^2+48N^4+48N^3Z-36N^2Z^2\\ \quad +96NZ+192N^2-48Z^2+256)\\ \left(4N^6Z+48N^4Z+192N^2Z+256Z\right)\\ \left(N^6Z^2+12N^4Z^2+48N^2Z^2+64Z^2\right)\end{bmatrix} \tag{32}$$

References

1. Frazier OH: Ventricular assist devices and total artificial hearts—A historical perspective. *Cardiol Clin* 21:1–13, 2003.
2. Untaroiu A, Wood HG, Allaire PE, *et al*: Computational design and experimental testing of a novel axial flow LVAD. *ASAIO J* 51: 702–710, 2005.
3. Giersiepen M, Wurzinger LJ, Opitz R, Reul H: Estimation of shear stress-related blood damage in heart valve prostheses—in vitro comparison of 25 aortic valves. *Int J Artif Organs* 13:300–306, 1990.
4. Dixon SI, Hall CA: Two-dimensional cascades in, *Fluid Mechanics and Thermodynamics of Turbomachinery*, 6th ed. Burlington, MA: Elsevier, 2010.
5. Turton RK: Fundamental principles in, *Principles of Turbomachinery*, 2nd ed. London, UK: Chapman & Hall, 1995.
6. Hanselman DL: *Brushless Permanent Magnet Motor Design*, 2nd ed. Lebanon, OH: Magna Physics Publishing, 2006.
7. Bourque K, Dague C, Farrar D, *et al*: *In vivo* assessment of a rotary left ventricular assist device-induced artificial pulse in the proximal and distal aorta. *Artif Organs* 30: 638–642, 2006.